Research Paper

A Logic-Gated Modular Nanovesicle Enables Programmable Drug Release for On-Demand Chemotherapy

Longguang Tang[1,2], Zhen Yang[2], Zijian Zhou[2✉], Ying Ma[2], Dale O. Kiesewetter[2], Zhantong Wang[2], Wenpei Fan[2], Shoujun Zhu[2], Mingru Zhang[2], Rui Tian[2], Lixin Lang[2], Gang Niu[2], Xianzhong Zhang[1✉], and Xiaoyuan Chen[2✉]

1. State Key Laboratory of Molecular Vaccinology and Molecular Diagnostics & Center for Molecular Imaging and Translational Medicine, School of Public Health, Xiamen University, Xiamen 361102, China
2. Laboratory of Molecular Imaging and Nanomedicine, National Institute of Biomedical Imaging and Bioengineering, National Institutes of Health, Bethesda, MD 20892, USA

✉ Corresponding authors: Zijian Zhou (zijian.zhou@nih.gov); Xianzhong Zhang (zhongxzh@xmu.edu.cn); Xiaoyuan Chen (shawn.chen@nih.gov)

Abstract

It remains a major challenge to achieve precise on-demand drug release. Here, we developed a modular nanomedicine integrated with logic-gated system enabling programmable drug release for on-demand chemotherapy.

Methods: We employed two different logical AND gates consisting of four interrelated moieties to construct the nanovesicles, denoted as v-A-CED$_2$, containing oxidation-responsive nanovesicles (v), radical generators (A), and Edman linker conjugated prodrugs (CED$_2$). The first AND logic gate is connected in parallel by mild hyperthermia (*I*) and acidic pH (*II*), which executes NIR laser triggered prodrug-to-drug transformation through Edman degradation. Meanwhile, the mild hyperthermia effect triggers alkyl radical generation (*III*) which contributes to internal oxidation and degradation of nanovesicles (*IV*). The second AND logic gate is therefore formed by the combination of *I-IV* to achieve programmable drug release by a single stimulus input NIR laser. The biodistribution of the nanovesicles was monitored by positron emission tomography (PET), photoacoustic, and fluorescence imaging.

Results: The developed modular nanovesicles exhibited high tumor accumulation and effective anticancer effects both *in vitro* and *in vivo*.

Conclusions: This study provides a novel paradigm of logic-gated programmable drug release system by a modular nanovesicle, which may shed light on innovation of anticancer agents and strategies.

Key words: modular nanomedicine, logic-gated, nanovesicle, drug release, cancer therapy

Introduction

Because of the numerous physical and chemical characteristic that can be engineered into nanomaterials, the field of nanomedicine has exploited these materials for sensing environmental parameters, providing images of human diseases, and providing drug delivery [1-3]. As of 2016, more than 50 nanodrugs had been approved by the U.S. Food and Drug Administration (FDA) and another 77 were undergoing clinical trials [4]. Specifically for cancer therapy, nanomedicine has shown appreciable advantages over traditional medicine, for example, through prolonging circulation time and/or shielding systemically toxic drugs by integrating with stimuli-responsive release strategies [5-9]. Despite the

potential, many of these strategies have not resulted in prolonged patient survival. This lack of enhanced efficacy is thought to be due, in part, to the nonspecific drug release occurring in healthy tissues resulting in system toxicity [10, 11]. Therefore, there is a need to develop more advanced strategies of engineering therapeutic nanoparticles (NPs) where drug release is explicitly controlled to maximize drug utilization and minimize systemic side effects [12].

For purposes of controlling drug release, stimuli-responsive NPs have been engineered to recognize tumor-specific internal stimuli (*e.g.*, pH, redox state, and enzymes) and external stimuli (*e.g.*, heat, magnetic field, light, and ultrasound) [13-18]. These strategies enable tailored drug release profiles in a spatiotemporally controllable manner [19-23]. However, a major caveat is that although materials sensitive to single factor can facilitate therapeutic delivery to tumor sites, individual biomarkers are rarely unique to all tumor sites. For example, acidic pH and reducing conditions are also shared by the stomach [24] and intracellular milieu [11] of living subjects, respectively, leading to suboptimal selectivity for targeted drug delivery and drug release. To improve site specificity of drug release, logic-gated systems that respond only when presented with multiple inducements provide a promising solution [25-30]. Although it's still in its infancy, logic-gated systems have been emerging as a useful platform affording programmable drug release for cancer therapy [31-36].

Polymeric nanoparticles [37], including micelles [38], nanogels [39], and vesicles, have proved to be a viable nanotechnology platform for effective drug delivery as demonstrated by their use in a series of pharmaceutical products for more than 40 years [40]. In particular, polymeric vesicles (*e.g.*, polymersomes) have been extensively engineered with unique properties enabling simultaneous loading of both hydrophilic and hydrophobic molecules [41, 42]. Compared to widely investigated liposomes, polymersomes have increased mechanical robustness [43, 44]. Therefore, we anticipate that polymeric nanovesicles could be the preferred platform for integrating well-ordered logic-gated nanomedicine.

Here we present a logic-gated drug release nanoformulation that integrates both external stimulus and internal stimulus for controlled drug release and subsequent cancer treatment (Figure 1). Controlled drug release was accomplished by incorporation of a heat sensitive prodrug version of doxorubicin (DOX) and a vesicle structure sensitive to degradation by reactive oxygen species (ROS). The nanovesicles were manufactured by self-assembly of the ROS responsive amphiphilic block-polymer,

poly(propylene sulfide)-poly(ethylene glycol) (PPS-PEG).[42, 45] The hydrophobic DOX prodrug, denoted as CED_2, was prepared by conjugation of two molecules onto the dye croconaine (CR780) using an Edman linker [46, 47]. The prodrug and hydrophilic free radical precursor, 2,2′-azobis[2-(2-imidazolin-2-yl)propane] dihydrochloride (AIPH),[48] were loaded onto the membrane and into the inner space of nanovesicles (denoted as v-A-CED_2), respectively. Drug release is controlled by two logical AND gates constructed by four interrelated units. The first AND gate requires mild hyperthermia (***I***, generated by photothermal agent CR780 under external 808 laser stimulation) and acidic pH (***II***, provided by the tumor microenvironment) that converts the prodrug into DOX by Edman degradation. The second logical gate requires the heat generated by laser irradiation to generate radicals from the decomposition of AIPH (***III***) and subsequent radical-induced oxidation of the PPS-PEG that leads to nanovesicle degradation (***IV***) and release of drug into the tumor. In other words, upon NIR irradiation, the photothermal agent CR780 in the prodrug CED2 generates heat and elevates the temperature, which then activates AIPH to generate free radicals and subsequent radical-induced oxidation of the PPS-PEG. Overall, these processes lead to nanovesicle degradation and release of prodrug into the tumor cells. Finally, DOX are released from the prodrug under the tumor acidic microenvironment and mild hyperthermia through Edman degradation.

Methods

Measurement of photothermal effect of CED_2

Temperature increase was evaluated by a) irradiation of 200 µL solution (10% DMSO in PBS) containing various concentrations of CED_2 with an 808 nm NIR laser at 0.5 W / cm² for 5 min, or B) exposing 20 µM CED_2 to different power densities (0.1 – 2 W / cm²)of the NIR laser. Photothermal stability was evaluated by exposing the 20 µM to a NIR laser (0.5 W/cm²) for five cycles. The NIR laser power density was determined by a laser energy meter (Coherent Inc., CA, USA). An SC300 infrared camera was employed to record the real-time temperatures of the solutions.

Edman degradation behavior of CED_2 and CD_2

Solutions of CED_2 (1 mg/mL) were prepared at different pH values (5.0, 6.5, 7.4) in phosphate buffer (10% DMSO). The resulting solutions were heated at different temperatures (37, 42 and 50 ºC) for 10 min. After cooling to room temperature, the solution was filtered and the filtrate analyzed by HPLC (A: 50 mM ammonium acetate buffer; B: CH₃CN) at a flow rate of

1 mL/min according to the following gradient program: 0-2 min, 5% of B; 2-15 min, 5%-80% of B; 15-20 min, 80% of B; 20-25 min, 80%-5% of B. The ratio of the peak area for DOX divided by the sum of the peak areas for DOX plus CED2 times 100 is reported as the degradation percentage. For comparison, CD_2 was also dissolved in different pH (5.0, 6.5 and 7.4) phosphate buffer (10% DMSO) but all were heated at 50 °C for 10 min and then analyzed by HPLC.

Formation of PPS-PEG based vesicles

The formation of PPS-PEG based vesicles was followed by a general procedure of solvent exchange or thin film method. For the preparation of PPS-PEG only vesicles (denoted as v), amphiphilic PPS-PEG (5 mg) copolymers were dissolved in chloroform (3 mL), the chloroform allowed to evaporate onto a surface, and the dry samples were re-dispersed in distilled water (1 mL) by subsequent hydration and sonication (2 min).

Drug loading and release

Initially, CED_2 or CD_2 were dissolved in DMF (1 mg/mL) and AIPH was dissolved in distilled water (1 mg/mL) as stock solutions. During the self-assembly of PPS-PEG vesicles, the above solutions containing different formulations were applied to disperse different vesicle formulations. The v-A, v-A-CED2, v-A-CD2, v-CED2, and v-CD2 samples were purified by a centrifugal filter (Amicon Ultra, Millipore) and repeated for three times. The supernatant was collected and the concentration of residual non-encapsulated CED_2 or CD_2 measured by UV absorption; according to the UV absorption standard curve of DOX at 480 nm. The drug loading content (DLC) and loading efficiency (LE) were calculated according to the following equations:

$$\text{Mass of encapsulated drug} = \text{mass of fed drug} - \text{mass of residual drug in supernatant}$$

$$\text{DLC (\%)} = \text{mass of encapsulated drugs} / \text{mass of carriers and encapsulated drugs} \times 100\%$$

$$\text{LE (\%)} = \text{weight of encapsulated drugs} / \text{weight of fed drugs} \times 100\%$$

Drug release profiles of DOX from PPS-PEG based vesicles were performed either with or without the application of NIR laser irradiation (0.5 W/cm² for 5 min) in different pH solution (pH 5.0 or 7.4). After the irradiation, the sample was centrifuged to precipitate the vesicle and the released DOX concentration measured at 480 nm.
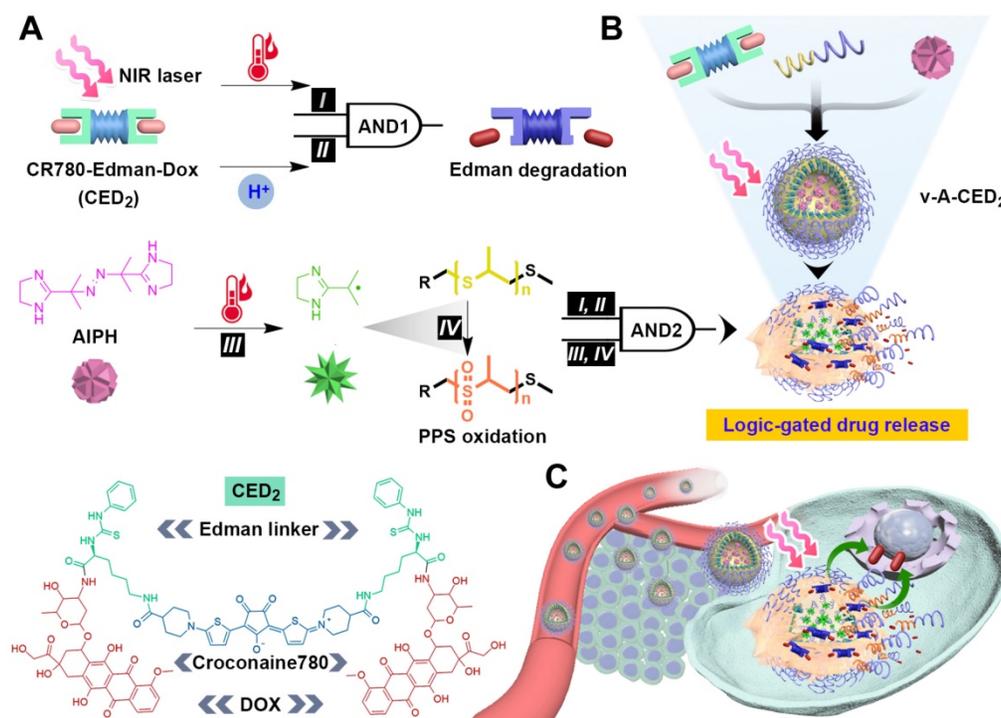
Figure 1. Schematic illustration of logic-gated drug release from the modular nanovesicles (v-A-CED2) for on-demand chemotherapy. A) Four units: mild hyperthermia (*I*, generated by photothermal agent CR780), acidic pH (*II*, tumor microenvironment), free radicals (*III*, from AIPH decomposition), and nanovesicle degradation (*IV*). The first AND logic (*I*, *II*) leads to prodrug-to-drug transformation through Edman degradation. The units *III* and *IV* cascade moieties cause oxidation and degradation of nanovesicles. The second AND logic combining *I-IV* leads to drug release from the nanovesicles. B) Self-assembly of amphiphilic polymer PPS-PEG, hydrophobic prodrug CED2, and hydrophilic component AIPH, forming v-A-CED2. Programmed drug release is achieved through a logic-gated mechanism external stimulus from a NIR laser. C) Schematic of NIR triggered drug release in a cell positioned in tumor microenvironment. The released DOX can enter cell nucleus and trigger cell death.

Generation of ABTS⁺·free radicals

The generation of ABTS⁺· was performed by taking advantage of the reaction between ABTS aqueous solution (2 mg/mL, 0.2 mL) and v-A aqueous solution (2 mg/mL, 0.2 mL). The mixture was protected from light irradiation and allowed to proceed for 0.5 h at 37, 42 or 50 °C. Then, the absorbance of diluted ABTS⁺·solution (with DI water) in the range from 400 nm to 950 nm was recorded using a UV-Vis spectrometer.

Cell viability assay

U87MG cells were seeded in a 96-well plate with a concentration of 1×10^4 cells/well. After 24 h incubation at 37 °C, various nanoparticle formations were added to each well in different concentrations (n = 3). NIR laser irradiation was conducted with 0.5 W/cm² for 5 min reaching about 42 °C or a higher optical power density (1 W/cm² for 5 min reaching about 50 °C). After 24 h, cell viability was evaluated using Cell Counting Kit-8 (CCK-8) method and calculated as percentages by referring to control (with or without NIR laser depending on experiments).

Reactive oxygen species detection *in vitro*

U87MG cells were seeded with a density of 5×10^5 per well in 12-well plates. After incubated for 24 h, the culture medium was replaced with 1 mL of fresh medium. Freshly prepared carboxy-H₂DCFDA was added into each well as loading solution with the final concentration of 2 µM and incubated for 20 min under cell culture condition. After washing by PBS for three times, cells were treated with various nanoparticle formations with or without laser irradiation (808 nm laser, 0.5 W/cm², 5 min) and allow for further incubation. Subsequently, the cells were washed with PBS and collected for flow cytometry study. Green fluorescence was recorded on the FL1 channel. All experiments were performed triply and independently with a total of 10^4 cells analyzed for each experiment.

Apoptosis assessment *in vitro*

Apoptosis rates were studied using R-phyco-erythrin (R-PE) annexin V and SYTOX green (Thermal Fisher Scientific) through flow cytometry following the manufacturer's instructions. Briefly, U87MG cells were stained with annexin-V conjugated to R-PE and SYTOX green for 15 min at 37 °C in a CO₂ incubator at 2 h after treated with different formulations and NIR laser irradiation (0.5 W/cm² for 5 min). SYTOX green fluorescence versus R-PE fluorescence was plotted and analyzed using CellQuest Pro software (BD Biosciences). All experiments were performed triply and independently with a total of 10^4 cells analyzed

for each experiment.

Radiolabeling and *in vitro* stability studies

^{64}CuCl₂ (222 MBq) was diluted in 2 mL of 0.1 M sodium acetate buffer (pH 5.5) and mixed with 50 µL of CED₂ (1mg/mL in aqueous solution with 10% DMSO). The reaction was incubated at 50 °C for 15 min and the labeling yield was evaluated by iTLC. For the preparation of ^{64}Cu-v-A-CED₂, the method was the same as the drug loading method. To test the stability of ^{64}Cu-v-A-CED₂ *in vitro*, it was incubated in PBS and mouse serum at 37 °C for 24 h.

MicroPET imaging

About 80 µCi of ^{64}Cu-v-A-CED₂ was intravenous injected into U87MG tumor-bearing mice and then were scanned at various time points with a micro PET(Siemens Inveon) scanner. The tumor uptake was calculated according to the 3-dimensional region of interests (ROIs) drawn on the tumor area in decay-corrected PET images.

In vivo photoacoustic and fluorescence imaging

All animal experiments were performed under the National Institutes of Health Clinical Center Animal Care and Use Committee (NIH CC/ACUC) approved protocol. The tumor model was established by subcutaneously injecting U87 MG cells (2×10^6) into the right back flank of mice (athymic nude, 5 weeks old). When the tumor size reached ~100 mm³, 100 µL of CED₂, v-A-CED₂ or v-A-CD₂ (0.5 mg/mL CED₂ or CD₂ content) was intravenously injected into the tumor-bearing mice (n = 3). Time points included one recording before injection (pre) and at 1 h, 4 h, 24 h, and 48 h after injection. The PA signals were performed by Visual Sonic Vevo 2100 LAZR system at a wavelength of 780 nm. The quantified PA intensities were obtained from the region of interests (ROIs).

In vivo thermal imaging

When the tumor size reached ~60 mm³, 100 µL of CED₂, v-A-CED₂ or v-A-CD₂ (corresponding to 100 µM CR780), was intravenously injected into the tumor-bearing mice. Thermal imaging was recorded by an SC300 infrared camera (FLIR) when the tumors were exposed to 808 nm laser (LASERGLOW Technologies) of power density at 0.5 W/cm².

In vivo tumor therapy study

After the tumor size reaching around 60 mm³, mice were randomly grouped into 7 groups (n = 5). The mice were intravenously injected with different formulations, including v-A-CD₂, v-A-CED₂, v-A, v-CED₂, free DOX, and PBS (2 groups), with a normalized dose of 4.0 mg/kg DOX (or equivalent amount of PPS-PEG if not applicable) per mouse.

After 24 h, 6 in 7 mice groups were treated with NIR laser irradiation (0.5 W/cm^2, 4 min), including v-A-CD$_2$ + L, v-A-CED$_2$ + L, v-A + L, v-CED$_2$ + L, free DOX + L and PBS + L. The tumor size and body weight were recorded every two days after each treatments until 14 days post-irradiation. Mice were euthanized when any dimension of tumor was close to 2 cm or when mouse body weight was lost by over 20%. The tumor volumes were calculated by the equation: V = width^2 × length/2. The survival rates were recorded until 40 days post-irradiation. Results were analyzed using GraphPad Prism 5 (La Jolla, CA).

Results and Discussion

Rational design and preparation of prodrug and nanovesicle to achieve logic-gated drug release system

To develop this nanomaterial, we first needed to prepare a pH and temperature labile prodrug. We selected CR780, as a linker between two molecules of DOX, because it has photothermal properties that would allow external laser irradiation to heat tissue. CR780 was conjugated to two molecules of lysine via the epsilon-amine. The alpha-amine was converted to a phenylthiourea and the lysine carboxylic acid conjugated with DOX (Scheme S1A) to give CED$_2$. We refer to the phenylthiourea moiety as an Edman linker because it can be degraded in response to dual stimuli of elevated temperature and acidic pH [49, 50]. For comparison purposes, CR780 conjugated DOX (CD$_2$), without the Edman degradable structure, was also synthesized by a direct one-step amide condensation (Scheme S1B). Chemical analyses of these compounds are presented in Figures S1-S9.

CED$_2$ and CD$_2$ showed similar absorption peaks with that of free DOX at 480 nm. However, the peak absorption of both CED$_2$ and CD$_2$ has a slight red shift compared with that of unmodified CR780 in the NIR region (Figure 2A). Similarly, a slight blue shift of fluorescence emission was found after conjugation (Figure S10). There was negligible change in NIR fluorescence intensity after modification (Figure S10). We also observed that CED$_2$ exhibited excellent photothermal stability after at least five cycles of NIR laser irradiation (808 nm, 0.5 W/cm^2) at pH 7.4 (Figure S11A). Meanwhile, the photothermal effect of CED$_2$ demonstrated a good linear dependence on its concentration and NIR laser power density (Figure 2B, Figure S11B-C), which allows for temperature-dependent degradation of CED$_2$.
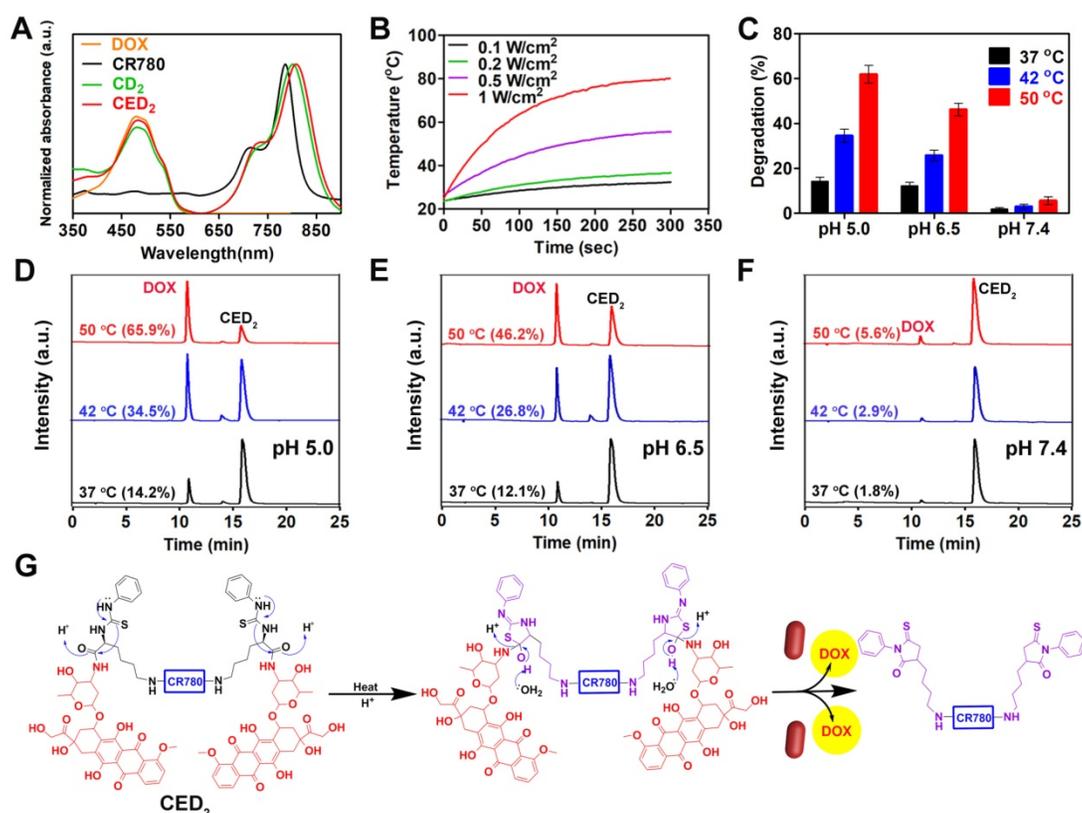

Figure 2. A) Normalized absorption spectrum of compounds before and after conjugation. B) Photothermal heating mediated by CED$_2$ (20 μM) as a function of laser power density for 5 min (808 nm). C) Area percent of DOX (480 nm, mean ± s.d., n = 3) following Edman degradation of CED$_2$ as a function of temperature and pH using a 10 min incubation. D-F) HPLC profiles (480 nm) of CED$_2$ following 10 min incubation in phosphate buffer solutions of different pH and temperature. G) The mechanism of Edman degradation of CED$_2$. The amide bond hydrolysis, assisted by low pH, elevated temperature, and by the participation of the neighboring thiourea group, results in the release of two-equivalents of DOX.

Since the Edman degradation depends on both temperature and pH (figure 2G), we evaluated the Edman degradation efficiency of CED_2 at different temperatures (37 °C, mild hyperthermia 42 °C, and hyperthermia 50 °C) and pH (5.0, 6.5 and 7.4). The degradation, expressed as the percent peak area of DOX at 480 nm, after a 10 min incubation are displayed in Figure 2C The amount of degradation was linearly correlated with both temperature and pH value. CED_2 showed less than 2% degradation under normal physiological conditions (37 °C, pH 7.4), indicating that even if CED_2 was released from the nanovesicles in normal tissues, it may not produce severe toxicity. However, the release of DOX reached about 30% at pH 6.5 when treated with mild hyperthermia (42 °C) for 10 min. On the other hand, the control compound CD_2 showed little to no degradation even after being treated with the harshest condition (50 °C, pH 5.0) for 10 min (Figure S11D). The degradation products were confirmed as DOX (MW calculated 543.52, found 544.19) and the expected side product croconaine-bis-phenylthiohydantoin (MW calculated 1018.30, found 1019.32) (Figure S12).

With prodrug in hand, we then constructed the nanomaterial to evaluate stimuli-responsive logic-gated drug release. The PPS-PEG copolymers were first synthesized according to literature procedures [45], and then self-assembled into nanovesicles with a size of around 100 nm. The transmission electron microscopy (TEM) image showed that the membrane thickness of the nanovesicles was about 6-8 nm (Figure 3A), and the overall hydrodynamic diameter

was around 100 nm from dynamic light scattering (DLS) analysis (Figure S13). During self-assembly of PPS-PEG copolymers, hydrophilic molecule AIPH was loaded into the interior cavity and hydrophobic prodrug CED_2 was encapsulated into the hydrophobic membrane of the nanovesicles simultaneously. The obtained v-A-CED_2 nanovesicles showed a dark contrast on the shell from the TEM image (Figure 3B), further indicating the successful encapsulation of CED_2 within the nanovesicles. For comparison purposes, different formulations including AIPH loaded nanovesicles (v-A), CED_2 encapsulated nanovesicles (v-CED_2), and AIPH, as well as CD2 co-loaded nanovesicles (v-A-CD2), were also prepared (Figure S14). We then studied the drug loading content (DLC) of the nanovesicles by using the weight fraction of CED_2. In a typical protocol, 10 mg of PPS-PEG polymer and 4 mg of CED_2 were used as starting materials for self-assembly which yielded a DLC of about 22.4% with a loading efficiency of about 83.7% in v-CED_2 samples. The remarkably high DLC in the v-CED_2 nanovesicles could be attributed to the hydrophobicity of CED_2 evidenced by the significant drop of solubility compared with CR780 or DOX alone. Additionally, v-A-CED_2 nanovesicles were obtained by a similar procedure to v-CED_2 but with the presence of 0.8 mg of AIPH, which turned into an AIPH loading content of about 3.7% and a loading efficiency of about 46.2%. The other nanovesicles, including v-A, v-CD_2, and v-A-CD_2, were prepared according to a similar protocol but using different starting materials.
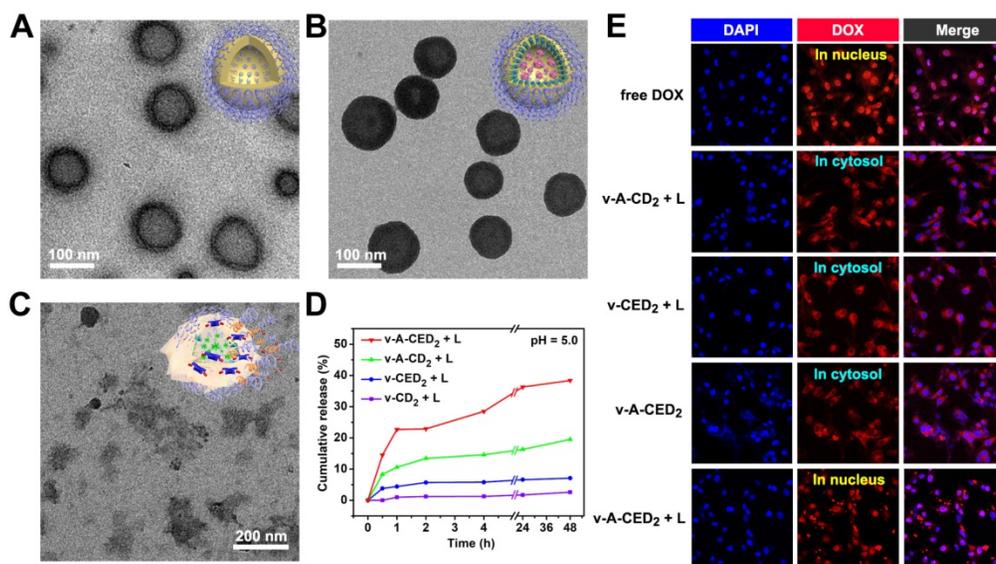
Figure 3. TEM images of nanovesicles: A) PPS-PEG only, B) v-A-CED_2, and C) v-A-CED_2 after incubation at 50 °C for 30 min. Insets are corresponding cartoons for the three kinds of nanovesicles. D) Cumulative drug release profiles of the various nanovesicles at pH5 following NIR laser irradiation to a temperature of about 42 °C (0.5 W/cm², 5 min). E) Confocal microscopy images of U87MG cells at 2 h after different treatments (L indicates irradiation with 808 nm laser at 0.5 W/cm² for 5 min). The signal from DOX accumulated in the nucleus of cells treated with free DOX or v-A-CED_2 + L, indicating the effective release of DOX from v-A-CED_2 + L. For the other four treatment groups, the signal of DOX was concentrated in cytosol, indicating negligible drug release from those nanovesicles.

Since drug release requires decomposition of the nanomaterial, we evaluated the decomposition of AIPH and v-AIPH (v-A) and measured the formation of free radicals as a function of temperature by measuring the absorption of 2,2′-azino-bis(3-ethylbenzothiazoline-6-sulfonic acid) free radicals (ABTS$^{+\bullet}$) at 500-950 nm. As shown in Figure S15, the generation of ABTS$^{+\bullet}$ was temperature-dependent when ABTS was incubated with AIPH and v(AIPH) (v-A) at 37, 42, and 50 °C. The amount of ABTS$^{+\bullet}$ at 50 °C was considerably higher than that at 42 and 37 °C, indicating much more free radicals generated by AIPH at a higher temperature. Notably, the generation of ABTS$^{+\bullet}$ from v-A was significantly lower than that from free AIPH, which can be attributed to the presence of PPS vesicles that consume free radicals. TEM image of v-A after incubation at 50 °C for 0.5 h showed significant degradation of the particle (Figure 3C), which was further confirmed by DLS measurement after NIR laser irradiation (Figure S16).

Evaluation of the logic-gated stimuli-responsive drug release of the nanovesicles *in vitro*

After validating the degradation behavior of CED$_2$ and nanovesicles, we sought to characterize the logic-gated stimuli-responsive drug release of the nanovesicles. Four kinds of nanovesicles (v-A-CED$_2$, v-A-CD$_2$, v-CED$_2$, and v-CD$_2$) were treated with different possible combinations of NIR laser and pH, and the cumulative drug release was measured using DOX fluorescence of the supernatant after ultra-centrifugation (figure 3D). When these vesicles were incubated in an acidic solution (pH 5.0) and treated with NIR laser until reaching 42 °C (0.5 W/cm^2, 5 min), v-A-CED$_2$ and v-A-CD$_2$ showed release of DOX within the first 1 h after NIR laser treatment, up to 25% and 10%, respectively (Figure 3D). Notably, drug release of the v-A-CED$_2$ gradually increased to 38% at 48 h after laser treatment, while the late-time drug release of v-A-CD$_2$ was minimal (less than 20%). In contrast, the v-CED$_2$ and v-CD$_2$ showed little drug release in response to NIR laser irradiation. The drug release for v-A-CED$_2$ and v-A-CD$_2$ at pH 7.4 may be attributed to free CED$_2$ and CD$_2$ released from nanovesicles, respectively (Figure S17A). The negligible difference was found between the conditions at pH 5.0 and 7.4 for samples without laser irradiation (Figure S17B and C). The prodrug CED$_2$ and the vesicles released very little DOX (< 5%) *in vitro* when incubated in mouse serum at 37 °C for 48 h (Figure S18). These results support that the drug release of v-A-CED$_2$ proceeds through a logic gated sequence. At the first AND gate, the simultaneous events of heating caused by NIR irradiation and low pH caused unmasking of the drug. At the second AND gate, the free radical released by NIR decomposition of AIPH and the presence of the oxidation-sensitive polymer vesicle, resulted in the release of anticancer drug into the tumor cell environment.

Using confocal microscopy, we observed the localization of DOX within U87MG cells following treatment of with the various vesicle formulations and laser treatment (Figure 3E). The confocal images showed that cells treated with v-A-CED$_2$ + L exhibited obvious accumulation of free DOX in nucleus owing logic-gated release following Edman degradation and vesicle rupture after NIR irradiation. All control vesicles showed fluorescence signal emitted by CED$_2$ (group v-CED$_2$ + L) or CD$_2$ (group v-A-CD$_2$ + L) in cytosol of cells.

Since our second logic-AND-gate requires the generation of free radicals to break down the vesicles and release drug, we evaluated the radical generation properties of the particles. As we expected, NIR laser irradiation of v-A-CED$_2$ produced the highest ROS level in cells (Figure 4A and 4B). We then quantified the cytotoxicity of different formulations with or without NIR laser irradiation against U87MG cells using cell counting kit 8 (CCK 8) assay. Cells were treated with v-A, v-A-CD$_2$, v-CED$_2$, v-A-CED$_2$ or free DOX at various concentrations normalized to the amount of DOX (or polymers) and with NIR irradiation (0.5 W/cm^2, 5 min, T = about 42 °C), and 24 hours later assayed for cell viability. v-A-CED$_2$ exhibited comparable cytotoxicity with free DOX but much higher cytotoxicity than control groups (Figure 4C). NIR irradiation did not cause any additional cytotoxicity under this mild hyperthermia. However, when treated with a higher optical power density NIR irradiation (1 W/cm^2 for 5 min) reaching about 50 °C, the v-A-CD$_2$ + L and v-CED$_2$ + L groups showed increased cytotoxicity that can be ascribed to the chemo-photothermal combination therapeutic effect (Figure S19A). Additionally, these nanovesicles, as well as the free prodrug CED2 without NIR laser irradiation, exhibited little to no cytotoxicity after 24 h incubation (Figure S19B). These results were confirmed by calcein AM and propidium iodide (PI) staining assay (Figure S20). Furthermore, we used Annexin V R-PE/SYTOX green to evaluate the apoptotic mechanism of cell killing effect by different formulations (Figure 4D). The results illustrated that cells treated with nanovesicles and laser irradiation underwent both apoptosis and necrosis, where v-A-CED$_2$ + L group showed significantly higher proportion of apoptotic (27.3%) and necrotic (47.5%) cell death (in total of 74.8%) under NIR laser irradiation than any of the control groups (Figure S21).
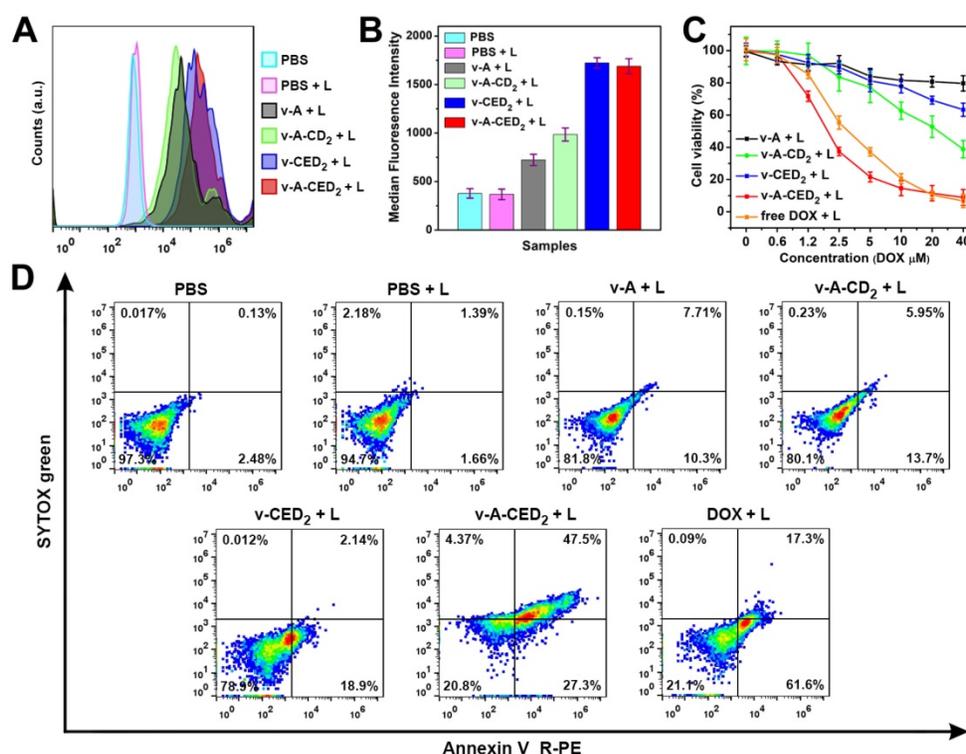
Figure 4. Cell studies (U87MG) of the various formulations treated with NIR laser (808 nm, 0.5 W/cm², 5 min). A) Flow cytometry analysis of ROS generation at 24 h. B) The corresponding median fluorescence intensity (MFI) derived from the flow cytometry results. Values are mean ± s.d. (n = 3). C) Cell viability assay at 24 h. D) Cells were stained with Annexin V R-PE/SYTOX green after 24 h incubation to evaluate apoptosis and necrosis.

Logic-gated drug release for on-demand chemotherapy guided by multimodality imaging

Encouraged by the promising *in vitro* cytotoxicity, we set out to explore *in vivo* applications. It is demonstrated that croconaine dyes can bind with divalent metal ions at the carbonyl oxygens [51], thus we sought to do the radiolabeling for CED₂ with ^{64}Cu, which enables quantitative pharmaco-imaging to monitor drug distribution *in vivo* by PET imaging. The radiochemical yield of ^{64}Cu-CED₂ is about 63% evaluated with instant thin layer chromatography (iTLC) (Figure S22A). Then the ^{64}Cu-v-A-CED₂ was obtained by self-assembling with PPS-PEG copolymers and AIPH, which was very stable in PBS and mouse serum (Figure S22B-22D), making it suitable for *in vivo* PET imaging. As shown in Figure 5A, the decay-corrected PET images displayed a high tumor-to-normal contrast. The quantification illustrated that the tumor accumulation of ^{64}Cu-v-A-CED₂ reached a peak (about 8% ID/g) at 24 h post-injection (Figure 5B). The concentration of ^{64}Cu-v-A-CED₂ in blood was obtained by quantifying the left ventricle from PET images, which illustrated that the radiotracer had a relatively long blood half-life (Figure S23). After the imaging, tumors and major organs were harvested for biodistribution study by gamma countering (Figure S24). We also evaluated

photoacoustic and fluorescence imaging of the v-A-CED₂, v-A-CD₂, and free CED₂ in a subcutaneous mouse tumor model as a measure of tumor uptake. As shown in Figure 5C-5F and Figure S25, the nanovesicles (v-A-CED₂) showed considerably higher tumor accumulation compared with CED₂, representing the good passive tumor targeting effect of the nanovesicles.

In subsequent *in vivo* studies, our logic-gated construction was evaluated in a xenografted mouse tumor model. Using a normalized dosage of DOX (4.0 mg/kg) (n = 5/group), the tumor temperature increase was monitor by NIR camera 24 hours post-injection of the various formulations during NIR irradiation (0.5 W/cm², 4 min). As expected, the temperature in the tumor of mice treated with v-A-CED₂, v-CED₂ or v-A-CD₂ rapidly increased to around 42 ℃ within 2 min. In contrast, the other groups (PBS, v-A, and free DOX) maintained the temperature at about 36 ℃ after laser irradiation (Figure 6A and 6B). Thus the photothermal properties of CR780 allow temperature elevation required for the logic-gated release of the drug.

In the continued evaluation of these vesicles for anti-tumor therapy (Figure 6C), favorable results were observed for the v-A-CED₂ + L group, where the tumor growth was effectively inhibited (97.0%). In comparison, both v-CED₂ + L and v-A-CD₂ + L groups

showed moderate tumor growth inhibition (44.8% and 27.1%, respectively), which can be explained by the lower efficacy of the AND gates since the lower temperature causes less prodrug release and less vesicle degradation. Moreover, the less effective tumor suppression of v-A-CD$_2$ + L than that of v-A-CED$_2$ + L clearly demonstrated the necessity of NIR triggered Edman degradation of drug release for effective cancer therapy. Correspondingly, mice treated with v-A-CED$_2$ + L exhibited the highest survival rate over other treatment groups, in which all the mice were alive for at least 40 days after treatment (Figure 6D). Furthermore, the hematoxylin and eosin (H&E) staining results also showed that tumors from the v-A-CED$_2$ + L group indicated greater apoptotic and necrotic tumor cell death compared to the other groups (Figure 6E). It should be noted that the other normal organ sections showed no obvious sign of damage (Figure S26). In addition, the low systemic toxicity was demonstrated by the maintenance of the body weights of the mice treated with nanovesicles (Figure S27).

Conclusions

In summary, we developed a novel approach to engineer modular nanomedicine with logic-gated responsiveness to environmental cues. The drug release was programmed by two different logical AND gates with four interrelated moieties, mild hyperthermia (*I*), acidic pH (*II*), free radicals (*III*), and the degradation of nanovesicles (*IV*). The external stimulus NIR-laser acted as the single input to activate these two logical AND gates. The established logic-gated modular platform showed effective anticancer efficacy both *in vitro* and *in vivo*. The nanovesicles (v-A-CED$_2$) significantly suppressed tumor growth in a subcutaneous xenograft model with a rate of 97% and prolonged the survival of mice. We anticipate that the strategy of developing modular nanomedicine may find great utility in targeted drug delivery and programmable drug release, as well as in applications for precision medicine.
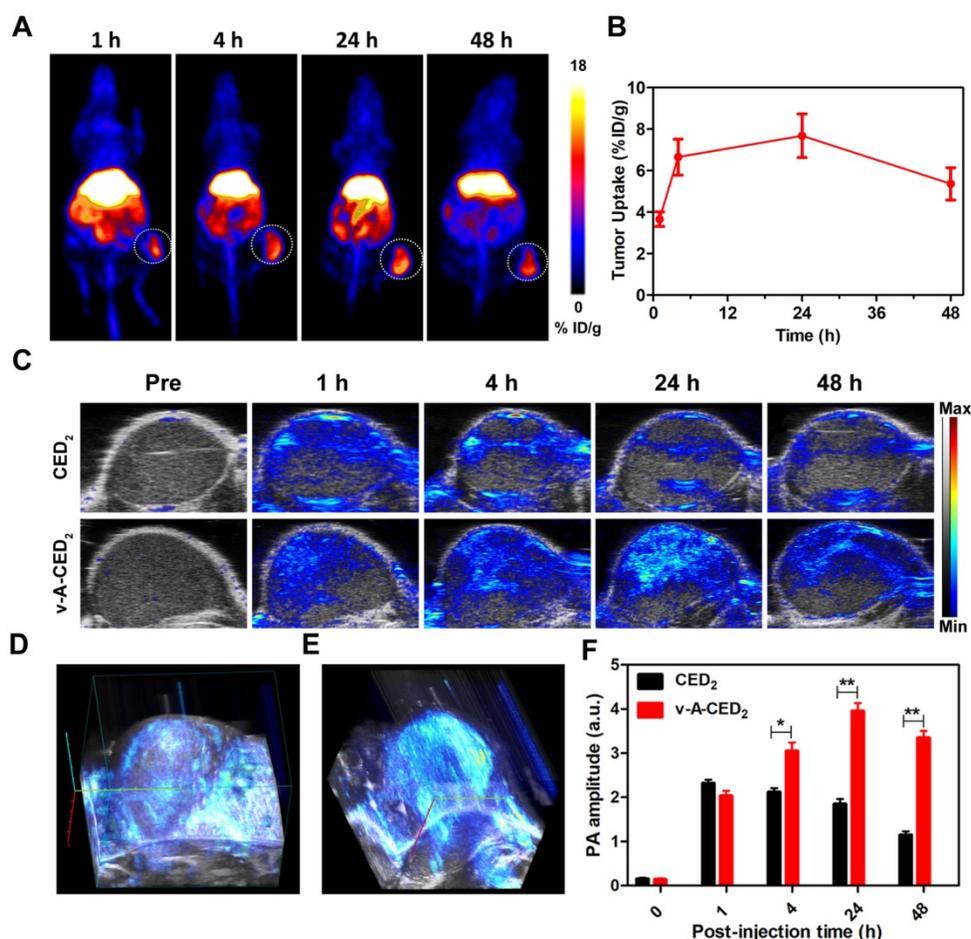
Figure 5. A) Representative PET images of U87MG tumor-bearing mice intravenously injected with ^{64}Cu-labeled v-A-CED$_2$ at different time points post injection. B) Drug accumulation in tumor quantified from decay-corrected PET images (n = 3). C) Photoacoustic/ultrasound co-registered images obtained at 780 nm before and 1 h, 4 h, 24 h, and 48 h after intravenous injection of CED$_2$ and v-A-CED$_2$ (100 uL, 0.5 mg/ml of CED$_2$ content) in U87MG tumor-bearing mice (n = 3). D) and E) 3D PA images of tumor tissues at 1 h p.i. of CED$_2$ and 24 h p.i. of v-A-CED$_2$, respectively. F) Corresponding quantification of PA signals of mice tumor region before and immediately, 1 h, 4 h, 24 h, and 48 h after intravenous injection of CED$_2$ and v-A-CED$_2$. *P<0.05, **P<0.01.
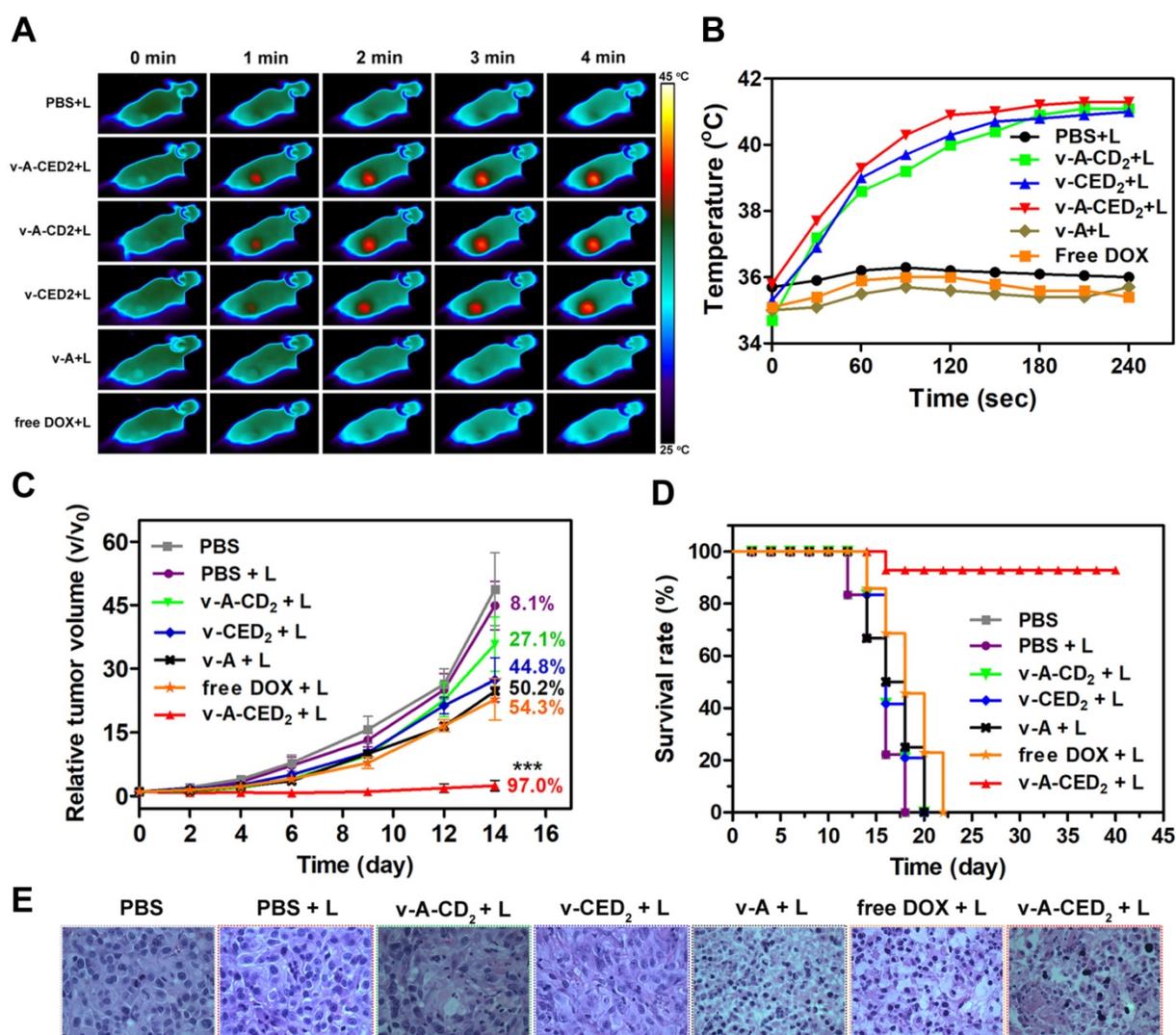
Figure 6. A) Thermal images of U87MG tumor-bearing mice i.v. treated with different samples and illuminated with 808 nm laser (0.5 W/cm², 4 min) at 24 h post-injection. B) Quantitative analysis of temperature changes in tumor area. C) Cancer therapy study in a U87MG subcutaneous mouse tumor model. NIR irradiation (0.5 W/cm², 4 min) was applied 24 h after i.v. injection of different formulations. Asterisks mark the significant differences between v-A-CED$_2$ + L and the other treatments (n = 5, ***P < 0.001). The numbers indicate the quantitative percentage (%) of tumor volume inhibition values for each group. D) Survival curves of tumor-bearing mice after various treatments. Note that the drop of survival rate for the v-A-CED$_2$ + L group at day 16 was due to mouse sacrificing for tissue collection for H&E staining. E) H&E analysis of tumor tissues after different treatments.

Abbreviations

PET: positron emission tomography; PA: photoacoustic imaging; DOX: doxorubicin; ROS: reactive oxygen species; NIR: near-infrared; TEM: transmission electron microscopy; DLS: dynamic light scattering; PBS: phosphate buffered saline; AIPH: 2,2′-azobis[2-(2-imidazolin-2-yl)propane] dihydrochloride; DLC: drug loading content; LE: loading efficiency. H&E: hematoxylin and eosin; ROIs: region of interests.

Acknowledgments

Supplementary Material

Supplementary figures.
http://www.thno.org/v09p1358s1.pdf

Competing Interests

The authors have declared that no competing interest exists.

References

1. Chen G, Roy I, Yang C, Prasad PN. Nanochemistry and Nanomedicine for Nanoparticle-based Diagnostics and Therapy. Chem Rev. 2016; 116: 2826-85.

2. Shi J, Kantoff PW, Wooster R, Farokhzad OC. Cancer nanomedicine: progress, challenges and opportunities. Nat Rev Cancer. 2017; 17: 20-37.
3. Pelaz B, Alexiou C, Alvarez-Puebla RA, Alves F, Andrews AM, Ashraf S, et al. Diverse Applications of Nanomedicine. ACS Nano. 2017; 11: 2313-81.
4. Bobo D, Robinson KJ, Islam J, Thurecht KJ, Corrie SR. Nanoparticle-Based Medicines: A Review of FDA-Approved Materials and Clinical Trials to Date. Pharm Res. 2016; 33: 2373-87.
5. Karimi M, Ghasemi A, Sahandi Zangabad P, Rahighi R, Moosavi Basri SM, Mirshekari H, et al. Smart micro/nanoparticles in stimulus-responsive drug/gene delivery systems. Chem Soc Rev. 2016; 45: 1457-501.
6. Chen H, Zhang W, Zhu G, Xie J, Chen X. Rethinking cancer nanotheranostics. Nat Rev Mater. 2017; 2: 17024.
7. Li X, Zheng BY, Ke MR, Zhang Y, Huang JD, Yoon J. A Tumor-pH-Responsive Supramolecular Photosensitizer for Activatable Photodynamic Therapy with MinimalIn VivoSkin Phototoxicity. Theranostics. 2017; 7: 2746-56.
8. Liu D, Yang F, Xiong F, Gu N. The Smart Drug Delivery System and Its Clinical Potential. Theranostics. 2016; 6: 1306-23.
9. Chen B, Dai W, He B, Zhang H, Wang X, Wang Y, et al. Current Multistage Drug Delivery Systems Based on the Tumor Microenvironment. Theranostics. 2017; 7: 538-58.
10. Hoffman AS. Stimuli-responsive polymers: biomedical applications and challenges for clinical translation. Adv Drug Deliv Rev. 2013; 65: 10-6.
11. Mura S, Nicolas J, Couvreur P. Stimuli-responsive nanocarriers for drug delivery. Nat Mater. 2013; 12: 991-1003.
12. Wang Y, Kohane DS. External triggering and triggered targeting strategies for drug delivery. Nat Rev Mater. 2017; 2: 17020.
13. Cheng R, Meng F, Deng C, Klok HA, Zhong Z. Dual and multi-stimuli responsive polymeric nanoparticles for programmed site-specific drug delivery. Biomaterials. 2013; 34: 3647-57.
14. Wen J, Yang K, Liu F, Li H, Xu Y, Sun S. Diverse gatekeepers for mesoporous silica nanoparticle based drug delivery systems. Chem Soc Rev. 2017; 46: 6024-45.
15. Dai Y, Xu C, Sun X, Chen X. Nanoparticle design strategies for enhanced anticancer therapy by exploiting the tumour microenvironment. Chem Soc Rev. 2017; 46: 3830-52.
16. Mai BT, Fernandes S, Balakrishnan PB, Pellegrino T. Nanosystems Based on Magnetic Nanoparticles and Thermo- or pH-Responsive Polymers: An Update and Future Perspectives. Acc Chem Res. 2018; 51: 999-1013.
17. Zhou Z, Song J, Nie L, Chen X. Reactive oxygen species generating systems meeting challenges of photodynamic cancer therapy. Chem Soc Rev. 2016; 45: 6597-626.
18. Liang X, Gao J, Jiang L, Luo J, Jing L, Li X, et al. Nanohybrid Liposomal Cerasomes with Good Physiological Stability and Rapid Temperature Responsiveness for High Intensity Focused Ultrasound Triggered Local Chemotherapy of Cancer. ACS Nano. 2015; 9: 1280-93.
19. Ruskowitz ER, Deforest CA. Photoresponsive biomaterials for targeted drug delivery and 4D cell culture. Nat Rev Mater. 2018; 3: 17087.
20. An X, Zhu A, Luo H, Ke H, Chen H, Zhao Y. Rational Design of Multi-Stimuli-Responsive Nanoparticles for Precise Cancer Therapy. ACS Nano. 2016; 10: 5947-58.
21. Wang Y, Deng Y, Luo H, Zhu A, Ke H, Yang H, et al. Light-Responsive Nanoparticles for Highly Efficient Cytoplasmic Delivery of Anticancer Agents. ACS Nano. 2017; 11: 12134-44.
22. Lei Q, Wang S-B, Hu J-J, Lin Y-X, Zhu C-H, Rong L, et al. Stimuli-Responsive "Cluster Bomb" for Programmed Tumor Therapy. ACS Nano. 2017; 11: 7201-14.
23. Yang K, Feng L, Liu Z. Stimuli responsive drug delivery systems based on nano-graphene for cancer therapy. Adv Drug Deliv Rev. 2016; 105: 228-41.
24. Bevan S, Geppetti P. Protons: small stimulants of capsaicin-sensitive sensory nerves. Trends Neurosci. 1994; 17: 509-12.
25. Douglas SM, Bachelet I, Church GM. A logic-gated nanorobot for targeted transport of molecular payloads. Science. 2012; 335: 831-4.
26. Ikeda M, Tanida T, Yoshii T, Kurotani K, Onogi S, Urayama K, et al. Installing logic-gate responses to a variety of biological substances in supramolecular hydrogel-enzyme hybrids. Nat Chem. 2014; 6: 511-8.
27. Chen X, Soeriyadi AH, Lu X, Sagnella SM, Kavallaris M, Gooding JJ. Dual Bioresponsive Mesoporous Silica Nanocarrier as an "AND" Logic Gate for Targeted Drug Delivery Cancer Cells. Adv Funct Mater. 2015; 24: 6999-7006.
28. Badeau BA, Comerford MP, Arakawa CK, Shadish JA, Deforest CA. Engineered modular biomaterial logic gates for environmentally triggered therapeutic delivery. Nature Chem. 2018; 10: 251-8.
29. Wang C, Sun W, Wright G, Wang AZ, Gu Z. Inflammation-Triggered Cancer Immunotherapy by Programmed Delivery of CpG and Anti-PD1 Antibody. Adv Mater. 2016; 28: 8912-20.
30. Liu X, Aizen R, Freeman R, Yehezkeli O, Willner I. Multiplexed Aptasensors and Amplified DNA Sensors Using Functionalized Graphene Oxide: Application for Logic Gate Operations. ACS Nano. 2012; 6: 3553-63.
31. Tregubov AA, Nikitin PI, Nikitin MP. Advanced Smart Nanomaterials with Integrated Logic-Gating and Biocomputing: Dawn of Theranostic Nanorobots. Chem Rev. 2018; 118: 10294-348.
32. Amir Y, Ben-Ishay E, Levner D, Ittah S, Abu-Horowitz A, Bachelet I. Universal computing by DNA origami robots in a living animal. Nat Nanotechnol. 2014; 9: 353-7.

33. Tang Y, Li Y, Hu X, Zhao H, Ji Y, Chen L, et al. "Dual Lock-and-Key"-Controlled Nanoprobes for Ultrahigh Specific Fluorescence Imaging in the Second Near-Infrared Window. Adv Mater. 2018; 30: 1801140.
34. Zhang X, Soh S. Performing Logical Operations with Stimuli-Responsive Building Blocks. Adv Mater. 2017; 29: 1606483.
35. You M, Zhu G, Chen T, Donovan MJ, Tan W. Programmable and multiparameter DNA-based logic platform for cancer recognition and targeted therapy. J Am Chem Soc. 2015; 137: 667-74.
36. Han H, Valdepérez D, Jin Q, Yang B, Li Z, Wu Y, et al. Dual Enzymatic Reaction-Assisted Gemcitabine Delivery Systems for Programmed Pancreatic Cancer Therapy. ACS Nano. 2017; 11: 1281-91.
37. Kamaly N, Xiao Z, Valencia PM, Radovic-Moreno AF, Farokhzad OC. ChemInform Abstract: Targeted Polymeric Therapeutic Nanoparticles: Design, Development and Clinical Translation. Chem Soc Rev. 2012; 43: 2971-3010.
38. Sun X, Wang G, Zhang H, Hu S, Liu X, Tang J, et al. The Blood Clearance Kinetics and Pathway of Polymeric Micelles in Cancer Drug Delivery. ACS Nano. 2018; 12: 6179-92.
39. Shi B, Huang K, Ding J, Xu W, Yang Y, Liu H, et al. Intracellularly Swollen Polypeptide Nanogel Assists Hepatoma Chemotherapy. Theranostics. 2017; 7: 703-16.
40. Elsabahy M, Heo GS, Lim SM, Sun G, Wooley KL. Polymeric Nanostructures for Imaging and Therapy. Chem Rev. 2015; 115: 10967-1011.
41. Palivan CG, Goers R, Najer A, Zhang X, Car A, Meier W. Bioinspired polymer vesicles and membranes for biological and medical applications. Chem Soc Rev. 2016; 45: 377-411.
42. Zhou Z, Chan A, Wang Z, Huang X, Yu G, Jacobson O, et al. Synchronous Chemoradiation Nanovesicles by X-Ray Triggered Cascade of Drug Release. Angew Chem, Int Ed. 2018; 130: 8599-603.
43. Discher BM, Won YY, Ege DS, Lee JC, Bates FS, Discher DE, et al. Polymersomes: tough vesicles made from diblock copolymers. Science. 1999; 284: 1143-6.
44. Photos PJ, Bacakova L, Discher B, Bates FS, Discher DE. Polymer vesicles in vivo: correlations with PEG molecular weight. J Control Release. 2003; 90: 323-34.
45. Napoli A, Valentini M, Tirelli N, Muller M, Hubbell JA. Oxidation-responsive polymeric vesicles. Nat Mater. 2004; 3: 183-9.
46. Tang L, Zhang F, Yu F, Sun W, Song M, Chen X, et al. Croconaine nanoparticles with enhanced tumor accumulation for multimodality cancer theranostics. Biomaterials. 2017; 129: 28-36.
47. Lynch DE, Hamilton DG. Croconaine Dyes – the Lesser Known Siblings of Squaraines. Eur J Org Chem. 2017; 2017: 3897-911.
48. Wang X, Gao F, Zhang X. Initiator-Loaded Gold Nanocages as a Light-Induced Free-Radical Generator for Cancer Therapy. Angew Chem, Int Ed. 2017; 129: 9157-61.
49. Lang L, Ma Y, Kiesewetter DO, Chen X. Stability analysis of glutamic acid linked peptides coupled to NOTA through different chemical linkages. Molecular pharmaceutics. 2014; 11: 3867-74.
50. Liu Y, Wang Z, Zhang H, Lang L, Ma Y, He Q, et al. A photothermally responsive nanoprobe for bioimaging based on Edman degradation. Nanoscale. 2016; 8: 10553-7.
51. Avirah RR, Jyothish K, Ramaiah D. Infrared Absorbing Croconaine Dyes: Synthesis and Metal Ion Binding Properties. The Journal of Organic Chemistry. 2008; 73: 274-9.